Experimental Investigation of a Cavitating Water Flow With the Addition of Drag-Reducing Agents

R. Azadi[1], and David S. Nobes[1*]
1: Dept. of Mechanical Engineering, University of Alberta, Canada
* Correspondent author: david.nobes@ualberta.ca

Keywords: PIV, PTV, cavitation, turbulence, drag reduction

ABSTRACT

Local reduction of the pressure in a flow field to levels lower than the saturation pressure triggers the production of tiny vaporous bubbles and causes the cavitation phenomenon. Higher pressure reductions significantly increase the cavitation bubbles' population, which can coalesce and generate large-scale cavitation structures such as cloud cavitation that shed downstream of the flow channel. The chaotic collapse of cavities produces strong shockwaves in regions with a recovered pressure which causes serious erosion on solid surfaces and high levels of noise. Hence, there is a growing interest in cavitation control methods. In this study, drag-reducing polymer additives are utilized as cavitation reducing (CR) agents in a converging-diverging mesoscale nozzle to verify the applicability of these agents in the control of the cavitation process. Analysis of high-speed images of the cavitating flow fields reveals that the viscoelastic flow of a 400 ppm polymer solution reduced the cavitation intensity by nearly 60 % relative to the pure water flow at a similar Reynolds number. Ultra-high-speed imaging of single cavitating bubbles at the inception showed that in a viscoelastic flow, the collapse period of cavities is longer, and their sizes are shrunk at a lower rate relative to their counterparts in the puer water. Particle image velocimetry (PIV) was used to study the near-wall turbulent flow fields at the flow conditions close to the cavitation inception, at different flow locations with non-zero pressure gradients present on the curved surfaces. Preliminary analysis of the results reveals that viscoelasticity alters the near-wall turbulence and distribution of the pressure gradient fluctuations, which might link to the significant reduction of cavitation intensity in polymeric flows.

1. Introduction

In a wall-bounded water flow, hydrodynamic cavitation is characterized by any local pressure decreasing to less than the saturation pressure at a known temperature. Pressure reduction triggers phase change and onsets the generation of steam bubbles or so-called *nuclei*. The main flow carries these micro cavitation bubbles downstream in the channel. Wherever the pressure recovers to more than the saturation pressure, the nuclei implode and generate relatively strong pressure bursts and shockwave fronts (Brennen, 2013). Cavitation intensity can be characterized by the cavitation number $\sigma = 2\,(P_{in} - P_{sat}) / (\rho\, U_{in}^2)$, where P denotes pressure and the subscripts

'in,' and 'sat,' stand for 'inlet,' and 'saturation'. Here ρ is the fluid density, and U_{in} is the area-averaged inlet velocity. A small increase in σ to more than the inception σ, rapidly increases the nuclei population in the flow field and generates cavitation clusters. These clusters are the large-scale features of the cavitating flow. The accumulation of cavitation clusters generates clouds for larger pressure drops that shed into the downstream flow (Arndt, 2002). For larger cavitation numbers, clouds grow largely in volume and fill in the decelerating flow zone, which results in choking. A cavitating flow encompasses high levels of turbulent fluctuations, phase change, and momentum transfer between two phases, making cavitation a complex phenomenon to study.

Micro cavitation can be advantageous in health applications such as cavitation-enhanced drug delivery in cancer therapy (Stride & Coussios, 2019). In industrial applications, cavitation usually causes erosion on the interacting solid walls by generating high-frequency pressure pulsations (Philipp & Lauterborn, 1998). Examples cover many industrial applications, such as cavitation on large-scale high-speed airfoils and ship hulls (Carlton, 2018) to smaller scales occurring in fuel injectors (Karathanassis, Hwang, Koukouvinis, Pickett, & Gavaises, 2021; Mitroglou, Stamboliyski, Karathanassis, Nikas, & Gavaises, 2017). It has been recently found that the addition of parts per million (ppm) of polymer additives or surfactants to the main flow has significant cavitation suppressing (CS) and cavitation reducing (CR) effects (Karathanassis et al., 2018; Naseri, Koukouvinis, Malgarinos, & Gavaises, 2018). High-speed X-ray imaging and numerical simulations conducted by Naseri et al. (2018b) show that adding 500 ppm of quaternary ammonium salt (QAS) viscoelastic additives to diesel fuel can suppress the cavitation bubble cloud and enhance the string cavitation regime.

Polymer additives and surfactants can significantly reduce the drag in turbulent flows with a high drag reduction (HDR) of up to 60% (Rajappan & McKinley, 2020; Warwaruk & Ghaemi, 2021; White & Mungal, 2008). Stretch of long-chain polymers with relaxation times larger than the turbulent time scale thickens the buffer layer, modifies the mean velocity profile, and results in a different wall shear stress distribution (White & Mungal, 2008). Warwaruk and Ghaemi (2021) showed that cationic surfactants produce lower initial DR and higher long-term DR for higher shear rates than polymer additives that mechanically degrade under continuous shear. The interaction between the turbulent flow field and the polymer additives or surfactant micelles is still not well understood and is an open research question.

There is a lack of sufficient evidence to elucidate the possible CR mechanisms of polymer additives and surfactants. In a cavitating flow of dilute additive solutions, local growth, accumulation, and transport of cavitation nuclei and their interaction with the turbulent boundary layer occur concurrently in the presence of long-chain molecules of polymers or surfactant micelles. At the

same time, these molecules or micelles undergo spatial and temporal elongations with varying shear rates in the flow field (White & Mungal, 2008).

The current work aims to develop a methodology based on an ultra-high-speed imaging system to interrogate water and dilute solution flow fields in the presence of cavitation. The method will help understand the effects of adding DR agents to a cavitating water flow and investigate any possible CR or CS mechanisms associated with these additives. A mesoscale converging-diverging flow channel with a throat size of 2 mm was designed for this purpose. Two-dimensional (2D) PIV was used to investigate the turbulent characteristics of the flow field. Ultra-high-speed imaging with frame rates up to one million frames per second was utilized to capture the cavitation regimes' temporal evolution and obtain time-resolved velocity fields. High-frequency pressure signals from the sensors installed downstream in the channel, and time-resolved ultra-high-speed images were utilized to quantify the strength of shockwaves propagating downstream on the midspan of the channel. The first phase of the experiments was devoted to validating the experimental methodology. The second phase focuses on determining the polymer additives' CR and CS effects by investigating the flow's turbulence and cavitation characteristics using ultra-high-speed imaging and is a work in progress.

2. Experimental procedure

2.1. Flow loop

A mesoscale flow loop was designed to examine the cavitation mechanism in a converging-diverging channel. A schematic of the experimental system is shown in Figure 1. A positive displacement pump (Model 33204; Moyno Inc.) delivers the flow to the test section via a contraction section. The contraction smoothly transforms the circular cross-section of the flow path into a rectangular entrance. As is illustrated in Figure 2(a), to straighten the incoming flow, a honeycomb was designed with uniformly distributed hexagonal hollows of inscribed circle diameter of 1.5 mm, with an edge-to-edge distance of 0.2 mm. The honeycomb has a length of 15 mm, and its outer face follows the internal topology of the contraction section at 75 mm from the test section's entrance.

Figure 2(b) illustrates that the fluid flow enters and exits the test section through a rectangular opening with a cross-sectional area of 10×5 mm^2 ($h_y \times h_z$). The width of the flow path was kept constant over the test section at $h_z = 5$ mm. The height decreases with a convergence angle of 60° over 5.2 mm. In the throat, height is constant, $h_t = 2$ mm, for a length of 5 mm. The channel's height

starts to increase smoothly again at a divergence angle of 12° over a length of 42.3 mm. The converging and diverging profiles of the flow path were generated based on a third-order polynomial profile, with their starting and ending points tangent to the horizontal flow path. Two transparent acrylic windows were installed on both sides of the channel to give optical access to the interior flow. The flow leaves the test section via a diffuser section, identical to the contraction.

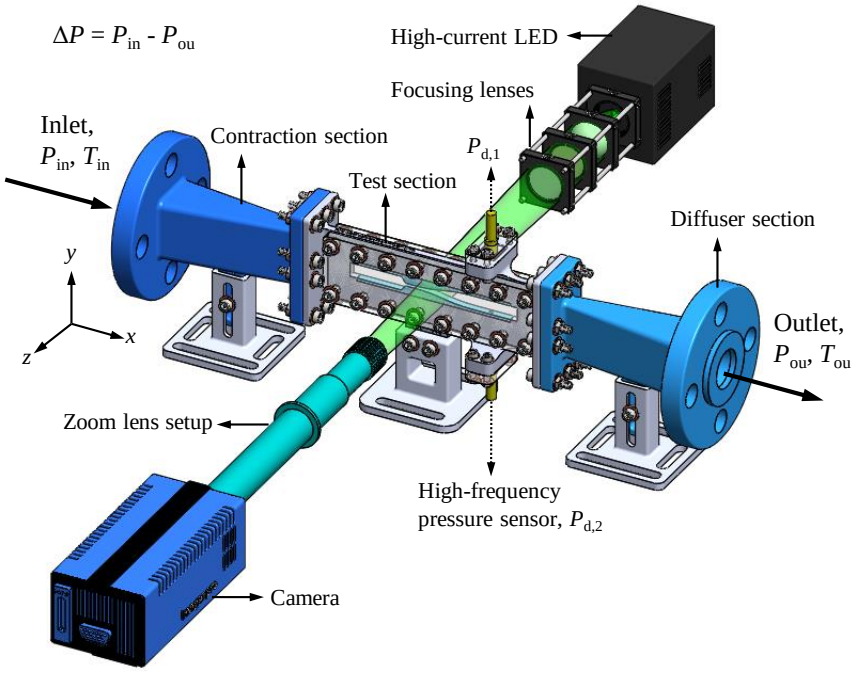

Figure 1: Schematic representation of the main components of the experimental system.

The contraction and diffuser sections, the honeycomb, the test section, and the converging-diverging nozzles were constructed using the low force stereolithography (LFS) technology (Form 3; Formlabs Inc.). Figure 2(b) shows that the nozzles can be easily separated from the test section and replaced with different nozzle shapes to generate different configurations, such as an asymmetric converging-diverging flow path. The nozzle surfaces were polished using ultra-fine micro-grit sandpapers, and the final surface finish was sufficiently smooth and glossy.

At the inlet and outlet of the test section, two differential pressure transducers (DP15; Validyne Engineering) were installed to measure the static gauge pressure of the flow at a scanning frequency of 1 kHz. The accuracy of the measurements was ±0.5 % FS. As shown in Figure 2(b), to measure the dynamic pressure fluctuations of the flow, two high-frequency quartz pressure sensors (112A05, charge type; PCB Piezotronics) were mounted in the downstream flow at the top and bottom of the test section. The scanning frequency of the pressure sensors was 125 kHz. Two resistance temperature detectors (RTDs) (TR40; WIKA Instruments Canada Ltd.) measured the incoming and outgoing flow temperatures. A custom code based on the data acquisition toolbox of MATLAB (2021, MathWorks) was developed to read, control, and store pressure and temperature signals.

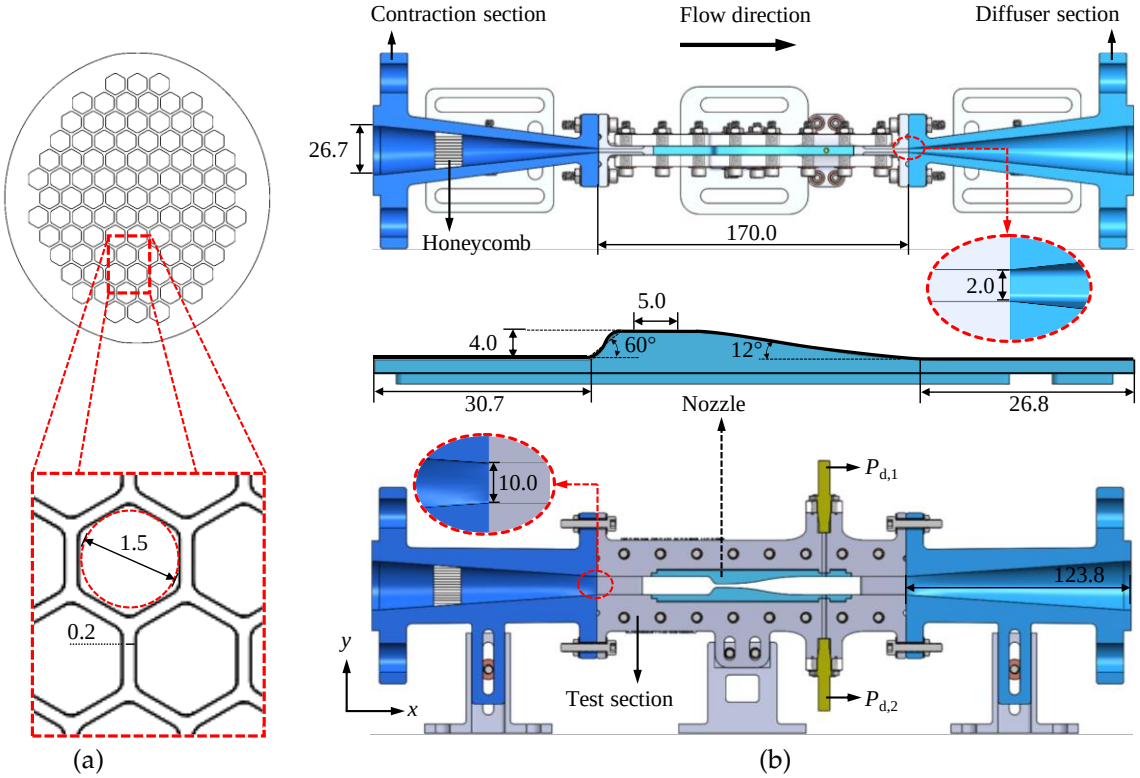

Figure 2: (a) Front view of the designed honeycomb with the main dimensions annotated on the zoomed view. (b) Schematic representation of the test section's main components. The top and bottom figures show cross-sections of the channel on central planes parallel to *xz* and *xy* planes, respectively. The nozzle profile is illustrated in the central figure. $P_{d,1}$ and $P_{d,2}$ denote the high-frequency pressure sensors installed downstream of the flow. All spatial dimensions are in mm. The throat height is h_t = 2 mm.

2.2. Imaging

As shown in Figure 1, the flow field was interrogated using an optical system based on backlit illumination. A green-light high-current LED (iLA.LPS v3; ILA_5150 GmbH) with a maximum frequency of 1 MHz illuminated the field-of-view (FOV). As illustrated in Figure 1, two bi-convex lenses were used in sequence. Their distances from the channel's central plane were carefully tuned to focus the light and uniformly distribute it on the relatively small FOVs to achieve the maximum intensity at higher frequencies. The liquid flow was seeded with silver-coated spheres of diameter 2 µm glass particles (Conduct-O-Fil® SG02S40; Potters Industries), which were continuously mixed in the reservoir using a magnetic stirrer (1103; Jenway).

A double-frame high-resolution camera (Image ProX4M; LaVision GmbH) with a pixel size of 7.4 µm recorded up to 5,000 pairs of images for each flow scenario. The camera and LED were synchronized and triggered via a high-speed programmable timing unit (PTU) system (LaVision GmbH). Depending on the maximum flow velocity in the FOV, the PTU generated a time interval of Δt_{piv} = 1.0 - 6.0 µs between the image frames. An ultra-high-speed camera (Hyper Vision HPV-

X2; Shimadzu Corporation) with frame rates up to 1 MHz was used to resolve the temporal evolution of cavitation structures in the channel downstream. The camera's full resolution is 400 × 250 pixels and can record up to only 128 frames in sequence, independent of the frame rate. The sensor pixels are rectangular with a size of 30.00 × 21.34 µm. Images of seeded flow were collected using the ultra-high-speed camera to perform time-resolved PIV.

A zoom lens (12X, 1-50486; Navitar Inc.) with an extension adapter (1X; 1-6015, Navitar) and a lens attachment (2X; 1-50015, Navitar Inc.) was used to obtain magnification factors more than unity. A micro-target plate (MP 50 × 12 µm; LaVision GmbH) with dot diameters in the range of 6.7 ± 1 µm to 100.0 ± 1 µm with dot distancing from 20 ± 1 µm to 300 ± 1 µm was used to calibrate the images. As highlighted in Figure 3, from the entrance region R0 to the separation region R5, the flow was examined in six different FOVs, comprising the flow behavior at the convergence, throat, divergence, and separation zones. Table 1 lists the sizes of the investigated FOVs and the main optical characteristics associated with each one.

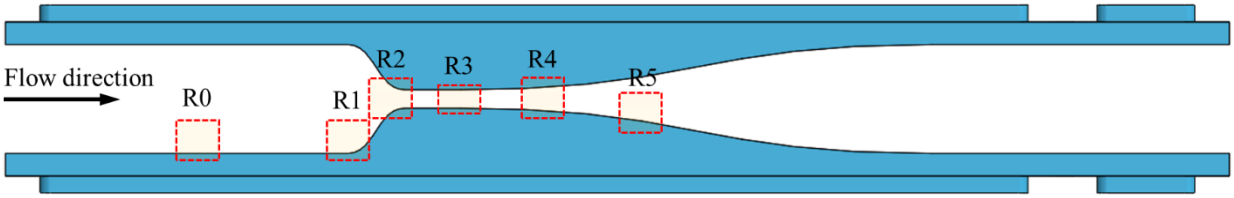

Figure 3: Investigated FOVs are highlighted in the flow region. R0, the entrance region, is located at ~ 15 mm from the end of the contraction. R1 and R2 cover the start and end of the convergence region. R3 is positioned approximately at the middle of the throat's flat plate. R5 interrogates the separation region, and its position depends on the applied flow conditions.

The formulation (Butterfield, 1978):

$$\delta_{\text{of}} = \frac{n\lambda}{(NA)^2} + \frac{ne}{M(NA)}, \tag{1}$$

was used to calculate the depth-of-field values shown in Table 1. Here, $n = 1$ is the refractive index of air, the medium between the lens and the object under study, $\lambda = 532$ nm is the wavelength of the green light, $e = 7.4$ µm is the discrete sensor size, and $NA = 0.11$ is the numerical aperture of the lens system.

Table 1: List of FOVs, shown in Figure 3, and their corresponding optical features.

Name	R0	R1	R2	R3	R4	R5
Width, h_x (mm)	2.18	2.18	2.19	2.18	2.18	2.19
Height, h_y (mm)	1.46	2.18	2.19	1.68	2.18	2.19
Magnificaton, M	6.97	6.94	6.94	6.96	6.95	6.98
Digital resolution, DR (µm / pixel)	1.062	1.064	1.064	1.062	1.064	1.060
δ_{of} (µm)	51.7	52.1	52.1	51.8	52.0	51.6

The mass flow rate was altered from 0.04 to 0.21 kg/s to generate various flow conditions. This range corresponds to average inlet gauge pressures of 2 kPa < P_{in} < 465 kPa for water and inlet

Reynolds numbers of Re_{in} ~ 6,000-10,000, where $Re_{in} = U_{in} D_{in} / \nu$. Here, D_{in} = 6.67 mm is the inlet's equivalent diameter, and ν is the kinematic viscosity of water. The MATLAB code 'XSteam' (Holmgren, 2021) was used to calculate the properties of water at different flow conditions.

2.3. Velocimetry processing

To improve the signal to noise ratio of the recorded images of the seeded flow field, (1) each image was inverted based on its maximum intensity, (2) a sliding Gaussian average with a filter length of 50 pixels was subtracted from the inverted image, and (3) the intensity of the resultant image was normalized by subtracting the average intensity from each pixel and dividing the resultant intensity by the standard deviation of that pixel. Each pair of images were iteratively cross-correlated based on a multi-pass configuration with decreasing interrogation window sizes to obtain the instantaneous velocity fields. 48 × 48 pixels windows were used in the first pass, and their size was reduced to 24 × 24 pixels to iterate for three more passes. The windows were ellipse in shape with a major to minor axis ratio of 2 oriented in the major flow direction. The overlap of the windows in all passes was 50 %. After each pass, the resultant velocity field was scanned to detect and remove universal outliers in a filter region of 5 × 5 pixels. A median filter was applied to the result to remove and replace any spurious vectors. Commercial software (DaVis V8.4; LaVision GmbH) was used for the PIV processing of the image data.

3. Results and discussion

Figure 4(a)-(f) illustrates instantaneous velocity fields of pure water flow at the channel's midspan in different FOVs highlighted in Figure 3. These results were obtained at the throat Reynolds number of $Re_{th} = 2.5 \times 10^4$, corresponding to the onset of cavitation in the experiments. Here, $Re_{th} = \rho U_{th} D_{th} / \mu_w$, where ρ is the liquid density, μ_w is the wall shear viscosity, is D_{th} the throat's hydraulic diameter, and U_{th} is the area-averaged throat velocity. The wall is outlined with black lines, and the wall area is colored grey. As shown in Figure 4(a)-(b), the near-wall velocity field is reasonably resolved in regions R0 and R1, where the water flows slowly compared to the throat, and the boundary layer is relatively thick. At R1, a favorable pressure gradient (FPG) drives the flow upstream.

At the throat's entrance (see Figure 4c), water flow accelerates rapidly, and, as shown in Figure 4(d), velocity increases to a maximum of 18 m/s in the throat. In this region, the boundary layer thickness is $\mathcal{O}$(10 μm), and we could not resolve it with the current optical settings. As Figure 4(e)

illustrates, the channel's height increases smoothly after the throat, the flow decelerates, and the boundary layer thickens. Here, the pressure gradient is adverse (APG), and as a result, the boundary layer separates, and the fluid counter flows upstream. Figure 4(f) shows an instantaneous velocity field of the separated boundary layer.

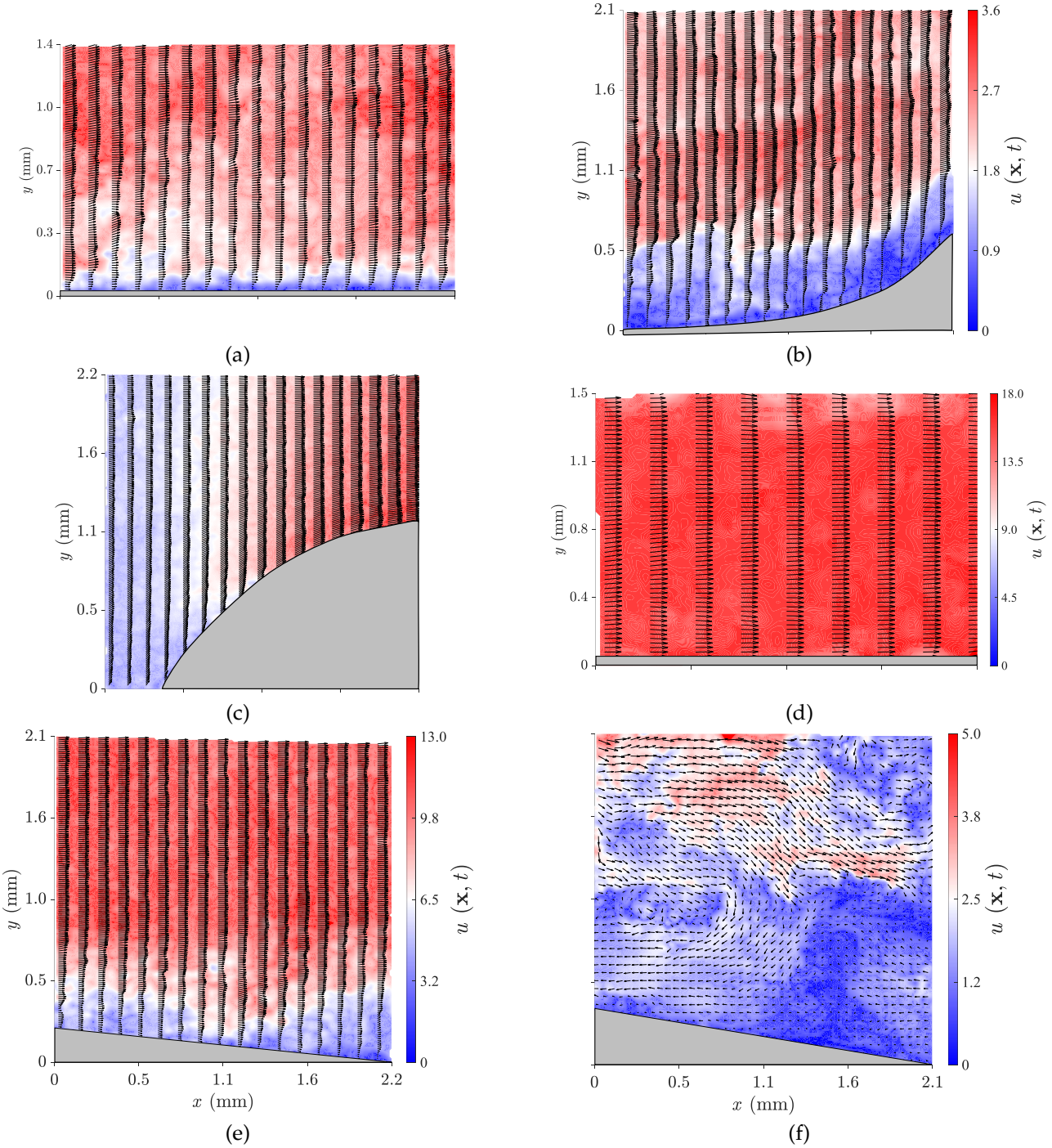

Figure 4: Instantaneous velocity fields at the onset of cavitation in water flow for the FOV (a) R0, near the entrance, (b) R1, the bottom of the convergence wall, (c) R2, entrance to the throat, (d) R3, throat, (e) R4, the exit of the throat, and (f) R5, in the separation region. Velocity vectors are imposed on the contour plots, colored in black, and are scaled according to the maximum velocity of each plot. Wherever required, velocity vectors are skipped for clarity. The channel's wall is highlighted in grey color.

The flow field was examined at the exit of the throat to capture the generated cavitation structures. Figure 5(a) shows that vapor bubbles coalesce in a pure water flow and develop into large shedding clouds at $Re_{th} = 3.8 \times 10^4$, $\sigma = 3.61$. Polyacrylamide (PAM) solutions in water were prepared at different concentrations to investigate the additives' CR or CS effects. A magnetic stirrer (1103; Jenway) mixed the solution batch for two hours before pumping it into the system. Each test solution was circulated at a moderate pump speed for 30 minutes before acquiring any data. Figure 5(b) illustrates instantaneous snapshots of a 200 ppm PAM solution flow at $Re_{th} = 3.6 \times 10^4$, $\sigma = 4.37$. Rheology measurements showed that the wall shear viscosity of the 200 ppm was × 1.4 of the water viscosity at the throat. A visual comparison of cavitation structures in Figure 5(a)-(b) shows that adding PAM additives reduces the cavitation intensity noticeably but does not entirely suppress it.

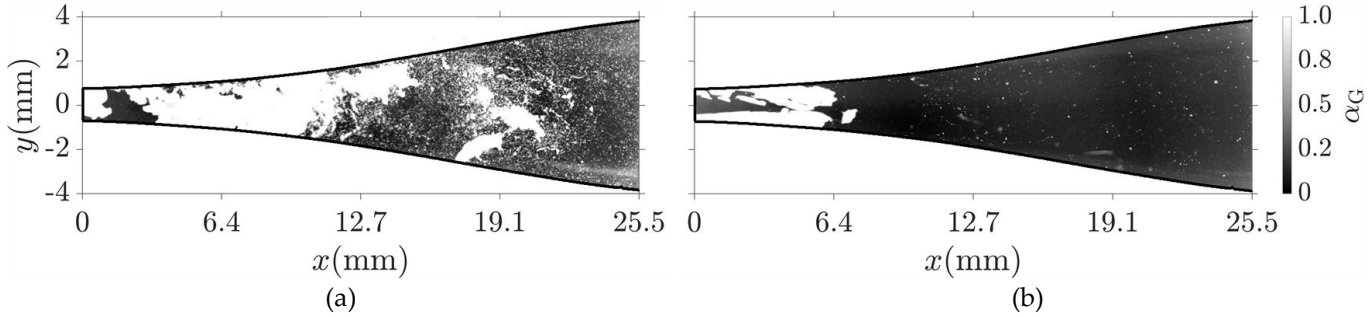

Figure 5:Instantaneous snapshots of cavitation structures for (a) water at $Re_{th} = 3.8 \times 10^4$, $\sigma = 3.61$, and (b) 200 ppm of PAM solution at $Re_{th} = 3.6 \times 10^4$, $\sigma = 4.37$. The bright regions in the images show the vapor phase, and the black areas illustrate the bulk flow. Here, α_G denotes the vapor ratio to the liquid at the imaged plane.

Spatiotemporal maps of the cavitating flows were obtained by averaging each image frame relative to the *y*-direction and stitching the resultant lines in time. Figure 6(a)-(b) illustrates the spatiotemporal maps of a cavitating pure water flow and a 400 ppm solution flow at a similar Reynolds number for $T = 0.9$ s. The addition of the polymeric additives significantly mitigates the fluctuations of the cavity closure by damping out their growth further downstream.

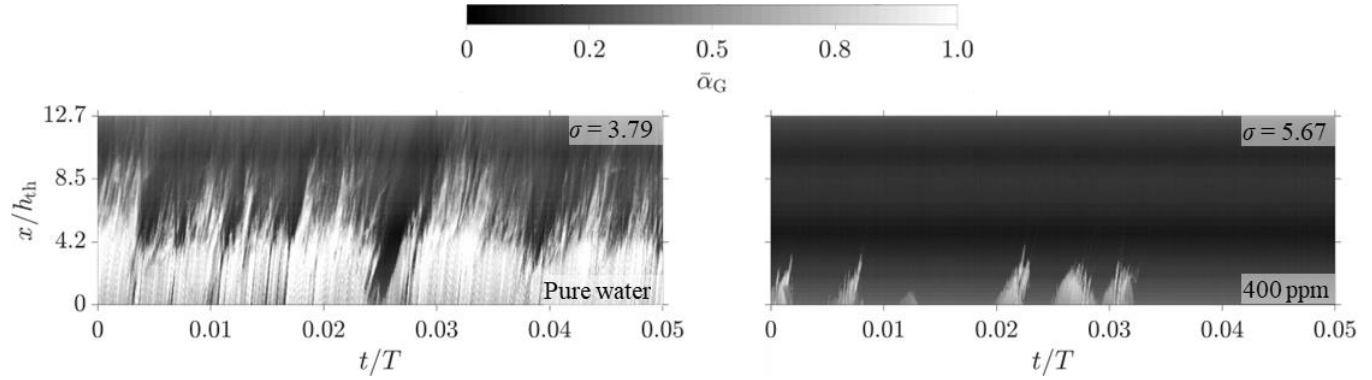

Figure 6: Spatiotemporal maps of cavitation structures for (a) pure water and (b) 400 ppm PAM solution at $Re_{th} = 3.4 \times 10^4$. The bright regions in the images show the vapor phase, and the black areas illustrate the bulk flow. Here, $\bar{\alpha}_G$ denotes the *y*-averaged vapor ratio to the liquid at the imaged plane.

The instantaneous turbulent PIV fields of pure water and two polymeric solutions of different concentrations are being analyzed to obtain the near-wall statistics, focusing on the FPG and APG regions. This investigation is a work in progress, and the detailed results will be presented on the conference day. The preliminary results elucidate that the viscoelasticity of the flow alters the local distribution of the mean and fluctuating pressure gradients, which might explain the different cavitation mechanisms in such viscoelastic flows.

Ultra-high-speed imaging was utilized to track the collapse of flowing single cavitating bubbles, with sizes in the order of 0.3 h_{th} (~ 0.6 mm) in pure water and different PAM solutions close to their inception points. An image processing algorithm developed in-house in MATLAB (Mathworks, 2022) (Azadi, Wong, & Nobes, 2020) was utilized to extract the instantaneous properties of the collapsing cavitation bubble, such as its equivalent radius R_b. Figure 7 shows the temporal variation of a collapsing cavitation bubble flowing in pure water and two PAM solutions with concentrations of 200 ppm and 400 ppm. The fastest collapse of the cavity occurs in water during a time interval of ~ 100 µs, before it starts to rebound. For the first 60 µs, the bubble's size shrinks at a constant rate of $dR_b/dt \sim 2.7$ m/s, after which the collapse process accelerates, and the shrinkage rate increases to $dR_b/dt \sim 9.8$ m/s.

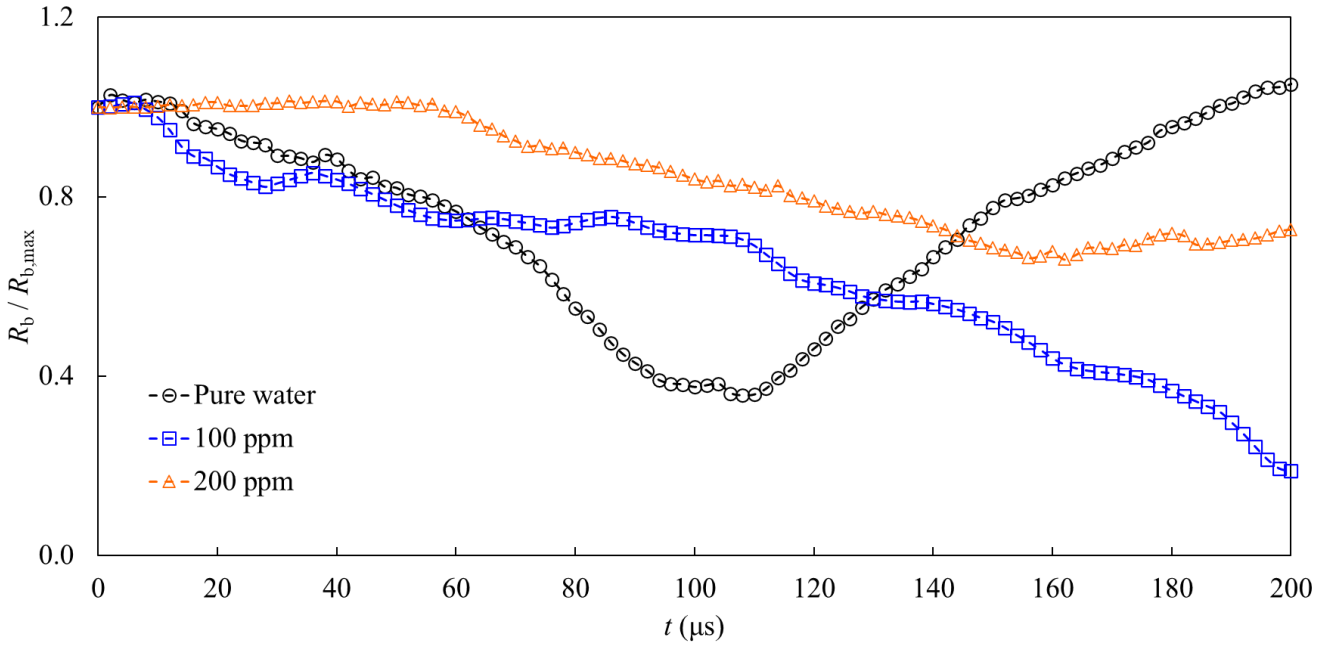

Figure 7: Temporal changes of the equivalent radius of cavitation bubbles R_b, normalized by its maximum radius in the analyzed time interval for pure water and two PAM solutions.

As Figure 7 illustrates, the cavitation bubble collapses in the polymeric solutions during longer periods compared to pure water. Until 200 µs recording of the collapse process, the 100 ppm did not start to rebound, and its shrinkage rate was ~ 1.7 m/s. Cavity maintains its size for ~ 60 µs while flowing in the 200 ppm solution, and after this instant, it starts to shrink at a rate of

~ 1.4 m/s. A viscoelastic polymeric flow relaxes the intensity of the collapse process by decelerating the cavities' shrinkage and extending the collapse period. Polymer molecules act as interconnected springs that store and release energy under compression and stretch and can modify the pressure field surrounding collapsing bubbles. Elucidation of this controlling behavior of the elastic polymer molecules may reveal how these additives reduce cavitation intensity. This is a work in progress, and we will present our updated findings on the conference day.

4. Conclusions

A mesoscale converging-diverging nozzle channel was designed to investigate the dynamics of cavitating flows in pure water and viscoelastic polymer flows. The main results can be listed as follows:

1- Spatiotemporal analysis of the high-speed images of cavitation structures elucidated that drag-reducing polymer additives mitigate the cavitation intensity and suppress the production of large-scale cavities at a concentration of 400 ppm.

2- Preliminary PIV investigation of the near-wall turbulent flow field at conditions close to the cavitation inception point revealed that the viscoelasticity of PAM solution flows alters the distribution of pressure gradient fields in regions with FPG and APG. As a result, the fluctuation of the pressure gradients might also change, which may link to the CR mechanism of polymer solutions.

3- The collapse histories of single flowing cavitation bubbles were tracked using ultra-high-speed imaging. It was revealed that cavities collapse at longer periods, with lower shrinkage rates relative to pure water. The surrounding viscoelastic flow, which alternatively stores and releases energy adjacent to the collapsing bubbles, is responsible for these alterations, which is being explored by the authors and is a work in progress.

Acknowledgments

The authors gratefully acknowledge financial support from Canada's Natural Sciences and Engineering Research Council (NSERC).

References

Arndt REA (2002) Cavitation in vortical flows. *Annual Review of Fluid Mechanics* 34:143–175.

Azadi R, Wong J, and Nobes DS (2020) Experimental and analytical investigation of meso-scale slug bubble dynamics in a square capillary channel. *Physics of Fluids* 32:083304.

Brennen CE (2013) *Cavitation and bubble dynamics Cavitation and Bubble Dynamics*. Cambridge: Cambridge University Press.

Carlton JS (2018) *Marine propellers and propulsion Marine Propellers and Propulsion*. Elsevier.

Karathanassis IK, Hwang J, Koukouvinis P, Pickett L, and Gavaises M (2021) Combined visualisation of cavitation and vortical structures in a real-size optical diesel injector. *Experiments in Fluids* 62:7.

Karathanassis IK, Trickett K, Koukouvinis P, Wang J, Barbour R, and Gavaises M (2018) Illustrating the effect of viscoelastic additives on cavitation and turbulence with X-ray imaging. *Scientific Reports* 8:14968.

Mitroglou N, Stamboliyski V, Karathanassis IK, Nikas KS, and Gavaises M (2017) Cloud cavitation vortex shedding inside an injector nozzle. *Experimental Thermal and Fluid Science* 84:179–189.

Naseri H, Koukouvinis P, Malgarinos I, and Gavaises M (2018) On viscoelastic cavitating flows: A numerical study. *Physics of Fluids* 30:033102.

Naseri H, Trickett K, Mitroglou N, Karathanassis I, Koukouvinis P, Gavaises M, … Wang J (2018) Turbulence and Cavitation Suppression by Quaternary Ammonium Salt Additives. *Scientific Reports* 8:1–15.

Philipp A, and Lauterborn W (1998) Cavitation erosion by single laser-produced bubbles. *Journal of Fluid Mechanics* 361:75–116.

Rajappan A, and McKinley GH (2020) Cooperative drag reduction in turbulent flows using polymer additives and superhydrophobic walls. *Physical Review Fluids* 5:114601.

Stride E, and Coussios C (2019) Nucleation, mapping and control of cavitation for drug delivery. *Nature Reviews Physics* 1:495–509.

Warwaruk L, and Ghaemi S (2021) A direct comparison of turbulence in drag-reduced flows of polymers and surfactants. *Journal of Fluid Mechanics* 917:A7.

White CM, and Mungal MG (2008) Mechanics and Prediction of Turbulent Drag Reduction with Polymer Additives. *Annual Review of Fluid Mechanics* 40:235–256.